Applied Mathematics and Computation 217 (2011) 9219–9233

Contents lists available at ScienceDirect

Applied Mathematics and Computation

journal homepage: www.elsevier.com/locate/amc

# An accurate numerical solution for the transient heating of an evaporating spherical droplet

S.L. Mitchell [a,*], M. Vynnycky [a], I.G. Gusev [b], S.S. Sazhin [b]

[a] Mathematics Application Consortium for Science and Industry (MACSI), Department of Mathematics and Statistics, University of Limerick, Limerick, Ireland
[b] Sir Harry Ricardo Laboratories, Centre for Automotive Engineering, School of Computing, Engineering and Mathematics, University of Brighton, BN2 4GJ, UK

ARTICLE INFO

*Keywords:*
Droplets
Diesel fuel
Heating
Evaporation
Stefan problem
Keller box scheme

ABSTRACT

A recently derived numerical algorithm for one-dimensional time-dependent Stefan problems is extended for the purposes of solving a moving boundary problem for the transient heating of an evaporating spherical droplet. The Keller box finite-difference scheme is used, in tandem with the so-called boundary immobilization method. An important component of the work is the careful use of variable transformations that must be built into the numerical algorithm in order to preserve second-order accuracy in both time and space – an issue not previously discussed in relation to this widely-used scheme. In addition, we demonstrate that our solution is in close agreement with the solution obtained using an alternative numerical scheme that employs an analytic solution of the heat conduction equation inside the droplet, for which the droplet radius was assumed to be a piecewise linear function of time. The advantages of the new method are discussed.



## 1. Introduction

Phase-change, or Stefan, problems, occur in a wide variety of natural and industrial processes. Mathematically, these are special cases of moving boundary problems, in which the location of the front between two material phases is not known beforehand, but must be determined as part of the solution. Although a few analytic solutions to such problems are known, it is more common to have to apply numerical methods [1]; amongst these are the boundary immobilization method [2–8], the enthalpy method [9,10], the variable space grid method [5,9], the finite element numerical method [11], the nodal integral method [12] and the heat balance integral method [10,13–20].

From amongst all of the above, the boundary immobilization method coupled to a Keller box discretization scheme of the one-phase one-dimensional time-dependent governing equations appears to perform best as regards order of accuracy and computational efficiency [7]. In particular, the algorithm was implicit, therefore not having any limitation on the time-step size, and was in addition shown to be second-order accurate in the time and space variables; all of the methods cited above are either of indeterminate accuracy or no higher than first-order accurate in time. Mitchell and Vynnycky [7] also resolved a further key issue regarding how to initiate a computation for a region which initially has zero thickness, as occurs in a wide range of Stefan problems. However, not all Stefan problems are of this type, and it is of interest to extend these methods to other applications. The particular subject of this paper is the evaporation of spherical fuel droplets, as occurs, for example, in Diesel engines [21–23].

Numerically speaking, the problem of droplet evaporation may seem no harder than the ones considered by Mitchell and Vynnycky [7]. However, as this paper will demonstrate, there are different issues that need to be resolved in order to produce

* Corresponding author.
*E-mail address:* sarah.mitchell@ul.ie (S.L. Mitchell).

0096-3003/$ - see front matter Crown Copyright © 2011 Published by Elsevier Inc. All rights reserved.
doi:10.1016/j.amc.2011.03.161

**Nomenclature**

*English*

| | |
|---|---|
| $a$, $b$ | coefficients introduced in Eq. (7) |
| $B_M$ | Spalding mass transfer number |
| $C_1$, $C_2$ | constants of integration given in Eq. (35) |
| $c$ | specific heat capacity, J kg$^{-1}$ K$^{-1}$ |
| $c_{gl}$ | dimensionless constant, $c_g/c_l$ |
| $D_1$, $D_2$ | constants of integration in Eq. (A7) |
| $E$, $\bar{E}$ | error estimates introduced in Section 4.2 |
| $F$ | $u/R(t)$ |
| $G$ | $F/\tau$ |
| $h$ | convective heat transfer coefficient, Wm$^{-2}$ K$^{-1}$ |
| $H$ | $\partial G/\partial\eta$ |
| $k$ | thermal conductivity, Wm$^{-1}$ K$^{-1}$ |
| $k_{gl}$ | dimensionless constant, $k_l/k_g$ |
| $L$ | specific heat of evaporation, J kg$^{-1}$ |
| $M$ | molar mass, kg mol$^{-1}$ |
| $p$, $\bar{p}$ | order of accuracy indices introduced in Section 4.2 |
| $P$ | pressure, Pa |
| $r$ | dimensionless distance from the centre of the droplet |
| $\bar{r}$ | distance from the centre of the droplet, m |
| $R$ | dimensionless droplet radius |
| $\overline{R}$ | droplet radius, m |
| $\mathcal{S}$ | location of moving boundary |
| $t$ | dimensionless time |
| $\bar{t}$ | time, s |
| $T$ | temperature, K |
| $u$ | $r\theta(r,t)$ |
| $X$ | time-like variable |
| $Y$ | space-like variable |
| $\mathcal{U}$ | temperature-like variable |
| $\mathcal{V}$ | $\partial\mathcal{U}/\partial Y$ |
| $\mathcal{Y}$ | mass fraction |

*Greek*

| | |
|---|---|
| $\alpha$ | exponent in Eq. (A1) |
| $\beta$ | dimensionless constant in Eq. (13) |
| $\gamma$ | dimensionless constant in Eq. (13) |
| $\Delta\eta$ | mesh size in the space-like variable $\eta$ |
| $\Delta\xi$ | mesh size in the space-like variable $\xi$ |
| $\Delta\tau$ | mesh size in the time-like variable $\tau$ |
| $\varepsilon$ | convergence criterion parameter |
| $\eta$ | independent variable, $(1-\xi)/t^{1/2}$ |
| $\eta_\infty$ | numerical value for the location of the outer edge of the lower deck |
| $\theta$ | dimensionless temperature |
| $\kappa$ | fuel thermal diffusivity ($k_l/\rho_l c_l$) |
| $\lambda$ | strictly positive constant introduced in Eq. (A1) |
| $\xi$ | $r/R(t)$ |
| $\rho$ | density |
| $\tau$ | time-like integration variable, $t^{1/2}$ |

*Subscripts*

| | |
|---|---|
| $e$ | evaporation |
| $f$ | fuel |
| $g$ | gas |
| $i$ | index for numerical spatial step |
| $j$ | mesh refinement index |
| $l$ | liquid |
| $m$ | index for iteration within each numerical time step |
| $s$ | surface |

| | |
|---|---|
| $v$ | vapour |
| 0 | initial value |

*Superscripts*

| | |
|---|---|
| $n$ | index for numerical time step |

a numerical scheme that is once again second-order accurate in both time and space. First of all, unlike the problems solved in [7], the solution domain is initially finite in extent and subsequently shrinks as the droplet evaporates. Thus, whilst similarity-like variables could be determined rather naturally in [7] for the purposes of initiating the numerical integration, the way to proceed for a spherical droplet is far from obvious; therefore, recourse to the physics of the problem, as well as to earlier work carried out in a different context [24], proves to be necessary for guidance. A related issue that we touch on here is whether all the dependent variables are solved for with the same accuracy: Mitchell and Vynnycky [7] only checked the order of accuracy of the numerical solution for the temperature, but since the temperature derivatives and the location of the front are also explicit variables of the numerical algorithm that are solved for, rather than determined by post-processing, it would make sense to determine the order of accuracy of those too.

In Section 2, we formulate a Stefan problem for the evaporation of a spherical droplet; in Section 3, we nondimensionalize the model equations and transform them to a form more suitable for numerical integration. The heart of the new material is given in Section 4, which explains how the Keller box scheme, in tandem with the boundary immobilization method, is applied to this particular problem. The results are then presented and discussed in Section 5, and conclusions are drawn in Section 6.

## 2. Problem formulation

Consider a liquid fuel droplet, initially of radius $R_0$ and at temperature $T_0$, immersed into a homogeneous hot gas at constant temperature, $T_g$, that is greater than $T_0$. Heat transfer within the droplet is assumed to occur by conduction alone; the effects of thermal radiation are ignored here, an assumption justified and discussed in more detail in [23]. At the surface of the droplet, evaporation and convection are assumed respectively to be the dominant cooling and heating mechanisms, and the radius of the droplet, $\overline{R}(\bar{t})$, is expected to decrease with time $\bar{t}$, if the effects of thermal swelling are ignored.

The droplet temperature, $T(\bar{r},\bar{t})$, is governed by the heat conduction equation in spherical coordinates,

$$\rho_l c_l \frac{\partial T}{\partial \bar{t}} = \frac{k_l}{\bar{r}^2}\frac{\partial}{\partial \bar{r}}\left(\bar{r}^2\frac{\partial T}{\partial \bar{r}}\right), \quad 0 \leqslant \bar{r} < \overline{R}(\bar{t}), \quad 0 \leqslant \bar{t} \leqslant \bar{t}_e, \tag{1}$$

where $\bar{r}$ is the distance from the centre of the droplet, $c_l$ is the specific heat capacity of the liquid, $k_l$ is its thermal conductivity and $\rho_l$ its density; for brevity, we introduce $\kappa = k_l/\rho_l c_l$ as the thermal diffusivity of the liquid fuel. In addition, $\bar{t}_e$ is the time taken for the droplet to evaporate completely.

Initial conditions are required at $\bar{t} = 0$ and boundary conditions are required at $\bar{r} = 0$ and $\overline{R}(\bar{t})$. For the former, we set

$$T(\bar{r},0) = T_0, \quad \overline{R}(0) = R_0, \tag{2}$$

where $T_0$ is constant, whereas the boundary condition at $\bar{r} = 0$ is simply

$$\frac{\partial T}{\partial \bar{r}}(0,\bar{t}) = 0. \tag{3}$$

Strictly speaking, we do not need to impose the boundary condition at $\bar{r} = 0$, as this is an internal point in the domain $\bar{r} \leqslant \overline{R}$; instead, we can look for the solution of Eq. (1) in the form of a twice continuously differentiable function $T \equiv T(\bar{r},\bar{t})$ for $0 \leqslant \bar{t} < \bar{t}_e$, $0 \leqslant \bar{r} < \overline{R}(\bar{t})$ [23]. However, a numerical scheme will require quantitative input at $\bar{r} = 0$, and (3) is the most appropriate, since it expresses spherical symmetry and ensures that the temperature will be bounded at $\bar{r} = 0$.

At $\bar{r} = \overline{R}(\bar{t})$, equating the conductive heat flux to the heat lost due to convective and evaporative cooling gives

$$k_l\frac{\partial T}{\partial \bar{r}} + h(T - T_g) = \rho_l L\dot{\overline{R}}(\bar{t}), \tag{4}$$

where $L$ is the specific heat of evaporation and $h(\bar{t})$ is the convection heat transfer coefficient, defined by $h(\bar{t}) = k_g/\overline{R}(\bar{t})$, with $k_g$ as the thermal conductivity of the gas. Note that the dot denotes differentiation with respect to $\bar{t}$. The above-mentioned expression for $h$ is valid when the droplets are stationary and the convection process in the gas phase reduces to a pure conduction process. The above approach can be generalised to the case of moving droplets within the so-called effective thermal conductivity model when $k_l$ in Eq. (1) is replaced with the effective conductivity $k_{\text{eff}}$ [22]. The moving boundary at $\bar{r} = \overline{R}(\bar{t})$ is controlled by fuel vapour diffusion from the droplet surface, and satisfies [22]

$$\dot{\overline{R}} = -\frac{k_g \ln(1 + B_M)}{\rho_l c_g \overline{R}}, \tag{5}$$

where $B_M = \mathcal{Y}_{fs}/(1-\mathcal{Y}_{fs})$ is the Spalding mass transfer number, and $\mathcal{Y}_{fs}$ is the mass fraction of fuel vapour near the droplet surface:

$$\mathcal{Y}_{fs} = \left[1 + \left(\frac{P_g}{P_{fs}} - 1\right)\frac{M_g}{M_f}\right]^{-1}; \tag{6}$$

here, $P_g$ and $P_{fs}$ are the ambient gas pressure and the pressure of saturated fuel vapour near the surface of the droplet, respectively, and $M_g$ and $M_f$ are the molar masses of the gas, here assumed to be air, and fuel. The variable $P_{fs}$ is calculated from the Clasius–Clapeyron equation as

$$P_{fs} = \exp\left[a - \frac{b}{T_s - 43}\right], \tag{7}$$

where $a$ and $b$ are constants to be given for specific fuels and $T_s = T(\bar{R}(\bar{t}), \bar{t})$ is the surface temperature of the fuel droplet. When deriving Eq. (5), it was assumed that the lewis number is equal to 1 and vapour at the surface of the droplet is always saturated, and the molecules can move infinitely fast from liquid to gas to maintain this status. This assumption implies that (5) predicts the maximal possible evaporation rate; the actual evaporation rate, as predicted by a more rigorous kinetic model, can be up to about 5–10% less than the one predicted by (5) for small droplets having radii of about 5 μm, even in a very dense gas in Diesel engine-like conditions [25,26].

Since $P_{fs}$ involves $T_s$, we must solve the coupled Eqs. (1) and (5) to determine $T(\bar{r}, \bar{t})$ and $\bar{R}(\bar{t})$, using the initial and boundary conditions specified above.

## 3. Nondimensionalization and transformation

Although it is possible to proceed in dimensional variables, nondimensionalization gives greater insight into the solution prior to computation, so we follow this route instead. To do so, we write

$$r = \frac{\bar{r}}{R_0}, \quad R = \frac{\bar{R}}{R_0}, \quad t = \frac{\bar{t}}{R_0^2/\kappa},$$

$$\theta = \frac{T - T_0}{\Delta T}, \quad \theta_g = \frac{T_g - T_0}{\Delta T}, \quad \theta_s = \frac{T_s - T_0}{\Delta T},$$

where we have chosen the timescale $R_0^2/\kappa$ from the heat conduction Eq. (1) and the temperature scale $\Delta T = L/c_l$ from the boundary condition (4). Hence, we have

$$\frac{\partial\theta}{\partial t} = \frac{1}{r^2}\frac{\partial}{\partial r}\left(r^2\frac{\partial\theta}{\partial r}\right), \quad 0 \leqslant r < R(t), \quad 0 \leqslant t \leqslant t_e, \tag{8}$$

where $t_e = \bar{t}_e/(R_0^2/\kappa)$; the initial conditions are

$$\theta(r, 0) = 0, \quad R(0) = 1 \tag{9}$$

and the boundary conditions are

$$\frac{\partial\theta}{\partial r} + \frac{k_{gl}(\theta - \theta_g)}{R} = \dot{R}(t) \quad \text{at } r = R(t), \tag{10}$$

$$R\dot{R} = -c_{gl}k_{gl}\ln(1 + B_M) \quad \text{at } r = R(t), \tag{11}$$

$$\frac{\partial\theta}{\partial r} = 0 \quad \text{at } r = 0, \tag{12}$$

with $k_{gl} = k_g/k_l$, $c_{gl} = c_l/c_g$. The form of (6) is unchanged, although (7) now becomes

$$P_{fs} = \exp\left[a - \frac{\beta}{\theta_s + \gamma}\right], \tag{13}$$

where $\beta = b/\Delta T$, $\gamma = (T_d - 43)/\Delta T$.

Having nondimensionalized the governing equations, several features become apparent. Using Table 1, we obtain $\Delta T \sim 10^2$ K, which is the same as obtained in [23]. In addition, it is clear that doubling $R_0$ will increase the relevant process timescale fourfold, which is also evident from the computations in [23]. Also, we note that these equations do not contain any dimensionless parameters that depend on $R_0$; thus, once the solution to the canonical problem posed by Eqs. (8)–(12) has been found, it can be used for any value of $R_0$, without the need for any further computation.

Lastly, we make use of a transformation that is standard for problems posed in spherical geometries. After introducing the new variable $u = r\theta(r, t)$, the problem is transformed to a planar geometry; the heat conduction Eq. (8) can then be written as

**Table 1**
Model parameter values, as used in [23].

| Parameter | Typical value | Units |
|---|---|---|
| $a$ | 15.5274 | – |
| $b$ | 5383.59 | – |
| $c_l$ | 2400 | J kg$^{-1}$ K$^{-1}$ |
| $c_g$ | 1600 | J kg$^{-1}$ K$^{-1}$ |
| $k_g$ | 0.03 | Wm$^{-1}$ K$^{-1}$ |
| $k_l$ | 0.04 | Wm$^{-1}$ K$^{-1}$ |
| $L$ | $3 \times 10^5$ | J kg$^{-1}$ |
| $M_f$ | 0.180 | kg mol$^{-1}$ |
| $M_g$ | 0.029 | kg mol$^{-1}$ |
| $P_g$ | $3 \times 10^6$ | Pa |
| $R_0$ | $5 \times 10^{-6}$ | m |
| $T_0$ | 300 | K |
| $T_g$ | 1000 | K |
| $\rho_l$ | 700 | kg m$^{-3}$ |

$$\frac{\partial u}{\partial t} = \frac{\partial^2 u}{\partial r^2}. \tag{14}$$

The initial and boundary conditions, (9)–(12), are then

$$u(r,0) = 0, \quad R(0) = 1, \tag{15}$$

$$\frac{\partial u}{\partial r} + \frac{(k_{gl}-1)u}{R} = k_{gl}\theta_g + R\dot{R} \quad \text{at } r = R(t), \tag{16}$$

$$R\dot{R} = -c_{gl}k_{gl}\ln(1+B_M) \quad \text{at } r = R(t), \tag{17}$$

$$u = 0 \quad \text{at } r = 0. \tag{18}$$

The forms of the expressions for $B_M$ and $\mathcal{Y}_{fs}$ remain the same, but now

$$P_{fs} = \exp\left[a - \frac{\beta}{u_s/R + \gamma}\right], \tag{19}$$

where $u_s = u(R(t),t)$.

## 4. Numerical method

### 4.1. Discretization scheme

Here, it is convenient to transform the variables further, and we begin by immobilizing the moving boundary by introducing the variables

$$\xi = \frac{r}{R(\tau)}, \quad \tau = \sqrt{t}, \quad u(r,t) = R(\tau)F(\xi,\tau). \tag{20}$$

Then, Eqs. (14)–(18) become

$$2\tau\frac{\partial^2 F}{\partial \xi^2} = RR'F + R^2\frac{\partial F}{\partial \tau} - \xi RR'\frac{\partial F}{\partial \xi}, \tag{21}$$

$$2\tau\frac{\partial F}{\partial \xi} + 2\tau(k_{gl}-1)F = 2\tau k_{gl}\theta_g + RR' \quad \text{at } \xi = 1, \tag{22}$$

$$RR' = -2\tau c_{gl}k_{gl}\ln(1+B_M) \quad \text{at } \xi = 1, \tag{23}$$

$$F = 0 \quad \text{at } \xi = 0, \tag{24}$$

$$F(\xi,0) = 0, \quad R(0) = 1, \tag{25}$$

where $(\cdot)'$ denotes differentiation with respect to $\tau$. Note that the time transformation $\tau = \sqrt{t}$ turns out to be essential in order to ensure that the later numerical scheme is second-order accurate for all variables, namely the temperature, flux and droplet radius; this is examined further in Section 5.

Whilst we could attempt a Keller box discretization for these equations with $\xi$ and $\tau$ as the independent variables, extensive numerical experimentation indicated that the results would not be second-order accurate in both time and space variables, in a strict sense that will be briefly explained in Section 4.2. To achieve second-order accuracy, however, it turns out to be necessary to make the similarity transformation

$$\eta = \frac{1-\xi}{\tau}, \quad F = \tau G(\eta, \tau), \tag{26}$$

so that (21)–(25) become

$$G_{\eta\eta} = \frac{\tau}{2} RR' G + \frac{R^2}{2}(G + \tau G_\tau - \eta G_\eta) + \frac{1}{2}(1-\eta\tau) RR' G_\eta, \tag{27}$$

$$-G_\eta + (k_{gl} - 1)\tau G = k_{gl}\theta_g + \frac{1}{2\tau} RR' \quad \text{at } \eta = 0, \tag{28}$$

$$RR' = -2\tau c_{gl} k_{gl} \ln(1 + B_M) \quad \text{at } \eta = 0, \tag{29}$$

$$G = 0 \quad \text{at } \eta = 1/\tau. \tag{30}$$

At first sight, this appears to introduce problems in Eq. (30), since the extent of the solution domain is once again varying with the time-like variable; we will show, however, how this issue can be resolved.

First of all, we consider the behaviour of (27)–(30) as $\tau \to 0$, obtaining

$$G_{\eta\eta} = \frac{1}{2} G - \frac{1}{2}\eta G_\eta, \tag{31}$$

subject to

$$G_\eta = k_{gl}\left(c_{gl} \ln(1 + B_{M,0}) - \theta_g\right) \quad \text{at } \eta = 0, \tag{32}$$

$$G \to 0 \quad \text{as } \eta \to \infty, \tag{33}$$

with

$$B_{M,0} = \lim_{\tau \to 0} B_M = \frac{M_f}{M_g\left(P_g \exp\left[\frac{\beta}{\gamma} - a\right] - 1\right)}.$$

Eq. (31) has the general solution

$$G(\eta) = C_1 \eta + C_2\left(\mathrm{e}^{-\eta^2/4} + \frac{\sqrt{\pi}}{2}\eta \operatorname{erf}\left(\frac{\eta}{2}\right)\right), \tag{34}$$

where $C_1$ and $C_2$ are constants to be determined from boundary conditions (32) and (33); it is straightforward to obtain

$$C_1 = k_{gl}\left(c_{gl} \ln(1 + B_{M,0}) - \theta_g\right), \quad C_2 = \frac{2k_{gl}}{\sqrt{\pi}}\left(\theta_g - c_{gl} \ln(1 + B_{M,0})\right). \tag{35}$$

Also, since

$$RR' \sim -2\tau c_{gl} k_{gl} \ln(1 + B_{M,0}), \tag{36}$$

we can integrate once with respect to $\tau$ to obtain

$$\frac{R^2}{2} \sim \frac{1}{2} - \tau^2 c_{gl} k_{gl} \ln(1 + B_{M,0}), \tag{37}$$

whence

$$R \sim 1 - \tau^2 c_{gl} k_{gl} \ln(1 + B_{M,0}). \tag{38}$$

Thus, as $\tau \to 0$, there is no difficulty as such with (27)–(30), despite the fact that $\eta \to \infty$.

The key point to note, however, is that the overall situation is similar to that in [24,27], with a double-deck solution structure in $\xi$ being necessary. In fact, the transformation (26) accounts for the variables in the lower deck where $1 - \xi \sim \tau$, whereas in the upper deck, where $\xi \sim 1$, one would simply choose $\xi$ and $\tau$ as the independent variables. Fortunately, in this problem, there turns out to be no need to solve in the upper deck, since $G$ and $G_\eta$ will be exponentially small there. This can be seen from (34) and (35), which indicate, on using

$$\operatorname{erf}(\eta) = 1 - \frac{\mathrm{e}^{-\eta^2}}{\eta\sqrt{\pi}}\left\{1 - \frac{1}{2\eta^2} + O(\eta^{-4})\right\},$$

that

$$G \sim \frac{4k_{gl}}{\sqrt{\pi}}\left[\theta_g - c_{gl}\ln(1+B_{M,0})\right]\frac{e^{-\eta^2/4}}{\eta^2} \quad \text{as} \quad \eta \to \infty; \tag{39}$$

however, care is necessary with regard to the numerical implementation of (30).

To apply the box scheme, we rewrite (27) as a first-order system by setting $G_\eta = H$. For a general dependent variable $\Phi$ and general independent time- and space-like variables, $X$ and $Y$ respectively, we define the following finite difference operators:

$$\mu_X \Phi^{n+\frac{1}{2}}_{i+\frac{1}{2}} = \frac{\Phi^{n+1}_{i+\frac{1}{2}} + \Phi^{n}_{i+\frac{1}{2}}}{2}, \quad \delta_X \Phi^{n+\frac{1}{2}}_{i+\frac{1}{2}} = \frac{\Phi^{n+1}_{i+\frac{1}{2}} - \Phi^{n}_{i+\frac{1}{2}}}{\Delta X}, \tag{40}$$

$$\mu_Y \Phi^{n+\frac{1}{2}}_{i+\frac{1}{2}} = \frac{\Phi^{n+\frac{1}{2}}_{i+1} + \Phi^{n+\frac{1}{2}}_{i}}{2}, \quad \delta_Y \Phi^{n+\frac{1}{2}}_{i+\frac{1}{2}} = \frac{\Phi^{n+\frac{1}{2}}_{i+1} - \Phi^{n+\frac{1}{2}}_{i}}{\Delta Y}. \tag{41}$$

With $X = \tau$, $Y = \eta$, the box scheme applied to (27) therefore gives, for $n = 0,1,2,\ldots$,

$$\mu_\tau \delta_\eta G^{n+\frac{1}{2}}_{i+\frac{1}{2}} = \mu_\tau \mu_\eta H^{n+\frac{1}{2}}_{i+\frac{1}{2}}, \tag{42}$$

$$\begin{aligned}\mu_\tau \delta_\eta H^{n+\frac{1}{2}}_{i+\frac{1}{2}} = {} & \frac{1}{2}\left(\mu_\tau \tau^{n+\frac{1}{2}} \mu_\tau R^{n+\frac{1}{2}} \delta_\tau R^{n+\frac{1}{2}} + \left(\mu_\tau R^{n+\frac{1}{2}}\right)^2\right)\mu_\tau \mu_\eta G^{n+\frac{1}{2}}_{i+\frac{1}{2}} + \frac{1}{2}\mu_\tau \tau^{n+\frac{1}{2}}\left(\mu_\tau R^{n+\frac{1}{2}}\right)^2 \mu_\eta \delta_\tau G^{n+\frac{1}{2}}_{i+\frac{1}{2}} \\ & - \frac{1}{2}\left(\mu_\eta \eta_{i+\frac{1}{2}}\left(\mu_\tau R^{n+\frac{1}{2}}\right)^2 - \left(1 - \mu_\eta \eta_{i+\frac{1}{2}}\right)\mu_\tau R^{n+\frac{1}{2}} \delta_\tau R^{n+\frac{1}{2}}\right)\mu_\tau \mu_\eta H^{n+\frac{1}{2}}_{i+\frac{1}{2}},\end{aligned} \tag{43}$$

which holds for $i = 1,\ldots,I-1$. Boundary condition (30) is simply $G^n_I = 0$, for $n = 0,1,2,\ldots$, and condition (28) becomes

$$-\mu_\tau \tau^{n+\frac{1}{2}} \mu_\tau H^{n+\frac{1}{2}}_0 + (k_{gl} - 1)\left(\mu_\tau \tau^{n+\frac{1}{2}}\right)^2 \mu_\tau G^{n+\frac{1}{2}}_0 = k_{gl}\theta_g \mu_\tau \tau^{n+\frac{1}{2}} + \frac{1}{2}\mu_\tau R^{n+\frac{1}{2}} \delta_\tau R^{n+\frac{1}{2}}. \tag{44}$$

The box scheme discretization of the condition in (29) is

$$\mu_\tau R^{n+\frac{1}{2}} \delta_\tau R^{n+\frac{1}{2}} = -2c_{gl}k_{gl}\ln\left(1 + B^{n+\frac{1}{2}}_M\right)\mu_\tau \tau^{n+\frac{1}{2}}, \tag{45}$$

where

$$B^{n+\frac{1}{2}}_M = \frac{M_f}{M_g\left(P_g \exp\left[\frac{\beta}{\mu_\tau \tau^{n+\frac{1}{2}} \mu_\tau G_0^{n+\frac{1}{2}} + \gamma} - a\right] - 1\right)}.$$

Finally, the initial conditions come from (34)

$$G^0_i = C_1\eta_i + C_2\left(e^{-\eta_i^2/4} + \frac{\sqrt{\pi}}{2}\eta_i \operatorname{erf}\left(\frac{\eta_i}{2}\right)\right), \quad H^0_i = C_1 + C_2\frac{\sqrt{\pi}}{2}\operatorname{erf}\left(\frac{\eta_i}{2}\right). \tag{46}$$

In practice, a finite computational domain of extent $\eta_\infty$ is chosen, and it is clear that the numerical outer edge of the lower deck, at which $G = 0$, meets the boundary at $\xi = 0$ when $\tau = 1/\eta_\infty$; clearly, the larger we make $\eta_\infty$, the more appropriate it becomes to neglect the upper deck for $\tau < 1/\eta_\infty$. Subsequently, for $\tau > 1/\eta_\infty$, the numerical integration should be continued in $(\xi,\tau)$ variables, although we omit writing down the complete discretization here. The box scheme is applied to the system (21)–(24) with initial conditions coming from the solution in $(\eta,\tau)$ variables, after the appropriate transformation using (26). It makes sense to continue the computation using $\tau$ instead of $t$ as the time variable, and this is the reason we use $\tau$ in (21)–(25), rather than leaving in terms of $t$. A schematic of the computational domain and the mesh used is given in Fig. 1.

It should be noted that Eq. (43) involves $R^{n+1}$ and so it is necessary to solve a nonlinear equation at each timestep. This is achieved by iterating on $R$, using the value at level $n$ as a starting guess, and then updating from solving the quadratic equation in (45) for $R^{n+1}$ until some desired tolerance, $\varepsilon$, is reached. Denoting by $R^{n+1}_{(m)}$ the value for $R^{n+1}$ after $m$ iterations, the convergence criterion used is

$$\left|R^{n+1}_{(m+1)} - R^{n+1}_{(m)}\right| < \varepsilon. \tag{47}$$

This iteration procedure at each timestep is continued until $R^{n+1}$ first becomes negative; it is of course not, in general, possible to ensure that $R^{n+1}$ equals exactly zero, which would correspond to finding the exact value of $t_e$, although we discuss in Section 6 how this might be achieved. In all computations, we use $\varepsilon = 10^{-13}$; this leads to an iteration count until convergence of less than 10 for each value of $n$.

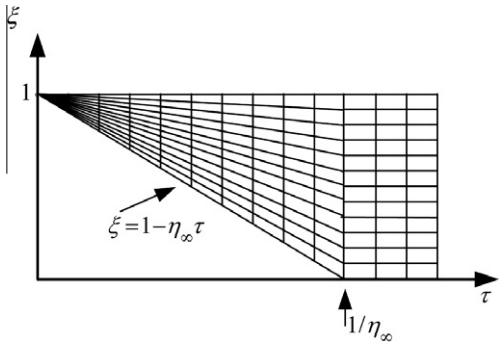


**Fig. 1.** Mesh for numerical scheme in $\xi$–$\tau$ variables.

### 4.2. Order of accuracy

We will also wish to determine the order of accuracy of our numerical scheme. We start this discussion by considering a sequence $\Delta Y_j$ where

$$\Delta Y_j = 2^{-j}\Delta Y_0, \quad j = 1,2,\ldots$$

and we denote the space coordinates of meshes associated with this sequence by

$$Y_{i,j} = i\Delta Y_j, \quad i = 0,1,\ldots,I_j, \quad j = 0,1,2,\ldots,$$

where

$$I_j = 2^j I_0, \quad j = 1,2,\ldots.$$

As discussed in [28], for a general numerical solution $U^n_{2^j i}$ and corresponding exact solution $\mathcal{U}(Y_{i,j}, X^n)$ to the heat conduction equation at the $n$th time-like step, $X^n$, the error and corresponding order of convergence, $E^n_{Uj}$ and $p_{Uj}$ respectively, are given by

$$E^n_{Uj} = \left(\Delta Y_j \sum_{i=0}^{I_0} \left(\mathcal{U}(Y_{i,0}, X^n) - U^n_{2^j i}\right)^2\right)^{1/2}, \quad p_{Uj} = \frac{\ln\left(E^n_{Uj}/E^n_{Uj+1}\right)}{\ln 2}, \tag{48}$$

for $j = 0,1,2,\ldots$ In order to be able to make use of (48), it is necessary that an exact solution is known. However, as demonstrated in [7], it turns out to be possible to estimate the order of accuracy even when an exact solution is not known. Instead of $E^n_{Uj}$ in (48), we define, for $j = 1,2,\ldots$

$$\bar{E}^n_{Uj} = \left(\sum_{i=0}^{I_0} \left(U^n_{2^j i} - U^n_{2^{j-1} i}\right)^2\right)^{1/2}, \quad \bar{p}_{Uj} = \ln\left(\bar{E}^n_{Uj}/\bar{E}^n_{Uj+1}\right)\Big/\ln 2; \tag{49}$$

in cases where an exact solution was known, Mitchell and Vynnycky [7] showed that $p_U = \bar{p}_U$, where

$$p_U = \lim_{j\to\infty} p_{Uj}, \quad \bar{p}_U = \lim_{j\to\infty} \bar{p}_{Uj}.$$

However, they applied this only to the temperature, i.e. $\mathcal{U}$; here, in contrast, we will apply it also to the spatial derivative of the temperature, $\partial\mathcal{U}/\partial Y$, and the location of the moving boundary which, for this general discussion, we denote by $\mathcal{S}(X)$. Thus, writing $\mathcal{V} = \partial\mathcal{U}/\partial Y$, we define, analogously to (48) and (49), for $j = 1,2,\ldots$

$$E^n_{Vj} = \left(\Delta Y_j \sum_{i=0}^{I_0} \left(\mathcal{V}(Y_{i,0}, t^n) - V^n_{2^j i}\right)^2\right)^{1/2}, \quad p_{Vj} = \frac{\ln\left(E^n_{Vj}/E^n_{Vj+1}\right)}{\ln 2}, \tag{50}$$

$$\bar{E}^n_{Vj} = \left(\sum_{i=0}^{I_0} \left(V^n_{2^j i} - V^n_{2^{j-1} i}\right)^2\right)^{1/2}, \quad \bar{p}_{Vj} = \ln\left(\bar{E}^n_{Vj}/\bar{E}^n_{Vj+1}\right)\Big/\ln 2, \tag{51}$$

$$E^n_{\mathcal{S}j} = \left|\mathcal{S}(X^n) - \mathcal{S}^n_j\right|, \quad p_{\mathcal{S}j} = \ln\left(E^n_{\mathcal{S}j}/E^n_{\mathcal{S}j+1}\right)\Big/\ln 2, \tag{52}$$

$$\bar{E}^n_{\mathcal{S}j} = \left|\mathcal{S}^n_j - \mathcal{S}^n_{j-1}\right|, \quad \bar{p}_{\mathcal{S}j} = \ln\left(\bar{E}^n_{\mathcal{S}j}/\bar{E}^n_{\mathcal{S}j+1}\right)\Big/\ln 2, \tag{53}$$

where $\left(V^n_{2^j i}, \mathcal{S}^n_j\right)$ and $(\mathcal{V}(Y_{i,j}, X^n), \mathcal{S}(X^n))$ denote, respectively, the numerical and exact solutions to the heat conduction equation at the $n$th time step; in addition, we define

$$\bar{p}_V = \lim_{j\to\infty} \bar{p}_{Vj}, \quad \bar{p}_{\mathcal{S}} = \lim_{j\to\infty} \bar{p}_{\mathcal{S}j}.$$

We point out that such a detailed investigation of the numerical accuracy of the Keller box method appears never to have been undertaken, not even in problems that were not moving-boundary problems; in fact, it appears that it was almost never necessary, although perhaps not for a reason that one might expect. Such problems had a self-similarity solution as the initial condition from which the solution evolves [29–31]; on the rare occasions that the scheme has been used for moving boundary problems, self-similar solutions were also available [6–8]. The only exceptions that we are aware of where there was no self-similarity solution was in fixed-boundary time-independent viscous boundary-layer computations by Cebeci et al. [27] and Vynnycky [24] in which, as usual, the streamwise space variable plays the role of a time-like variable: due to a discontinuity in a boundary condition, it was necessary to introduce a double-deck structure for the transverse space variable and to use numerical matching. For the current problem, therefore, it is necessary to consider whether there are any discontinuities, and hence inconsistencies, between the initial and boundary data at $\eta = 0$ as $\tau \to 0$ and $\tau = 0$ as $\eta \to 0$. Identifying $U$ with $G$, $V$ with $H$ and $\mathcal{S}$ with $R$, it is evident from the analysis in Section 4.1 that the data is consistent for $U$, but inconsistent for $V$, since we have that

$$U(\eta, 0) \to 0 \text{ as } \eta \to 0, \quad U(0, \tau) = 0 \text{ as } \tau \to 0, \tag{54}$$

but

$$V(\eta, 0) \to 0 \text{ as } \eta \to 0, \quad V(0, \tau) \nrightarrow 0 \text{ as } \tau \to 0. \tag{55}$$

Hence, had we solved the governing equations without the use of transformation (26), we would not expect to find that $\bar{p}_U = \bar{p}_V = \bar{p}_{\mathcal{S}} = 2$; using (26), however, should lead to this result, which is the motivation for introducing it in this paper. This is indeed borne out, although we do not display here the values obtained for $\bar{p}_U$, $\bar{p}_V$ and $\bar{p}_{\mathcal{S}}$ when (26) was not used. Note also that the discontinuity in Eq. (55) is not a consequence of transformation (26). First of all, if (26) is not used and we try to solve (21)–(25), we find that the problem is degenerate as $\tau$ tends to zero, since the highest order derivative is multiplied by $\tau$. It is therefore not possible to know from (21)–(25) whether there is a discontinuity or not. Furthermore, it should be noted that it would not have been possible to see whether there is a discontinuity from Eqs. (8)–(12), either, although there is no reason to believe that there would not be a discontinuity, since initial condition (9) and boundary condition (10) have been chosen independently of each other.

## 5. Results

In view of the canonical nature of the problem, it is more appropriate to present the results in terms of nondimensional variables.

First, we consider the numerical accuracy of the scheme. Table 2 compares the relevant values of $\bar{p}$ for a sequence of progressively finer meshes when using $\eta_\infty = 5$, 10 and 20 at $\tau = 0.4$; this value of $\tau$ was chosen as it is well before complete evaporation occurs, but nevertheless after the switch has been made from $(\eta, \tau)$-to $(\xi, \tau)$-coordinates. Note that these results come from solving (21)–(25), and we have used the notation $\widetilde{F} = \partial F/\partial\xi$. Table 3 shows the corresponding data at $\tau = 0.76$ which, as we will see later, is just prior to complete evaporation. From these tables, we see that $\bar{p}$ tends to 2 for all variables that are solved for, and that there is no deterioration in the accuracy as the extent of the droplet dwindles; thus, the scheme is second-order accurate in both time- and space-like variables.

**Table 2**
Order of accuracy for a sequence of meshes at $\tau = 0.4$.

| $\eta_\infty$ | $\bar{p}$ | $\Delta\eta$ ($j$) | | | |
|---|---|---|---|---|---|
| | | 1/8 (2) | 1/16 (3) | 1/32 (4) | 1/64 (5) |
| 5 | $\bar{p}_{Fj}$ | 1.99644 | 1.99907 | 1.99975 | 1.99993 |
| | $\bar{p}_{\widetilde{F}j}$ | 2.02469 | 2.00312 | 2.00020 | 2.00004 |
| | $\bar{p}_{Rj}$ | 1.98877 | 1.99710 | 1.99927 | 1.99982 |
| 10 | $\bar{p}_{Fj}$ | 2.00028 | 2.00006 | 2.00002 | 2.00001 |
| | $\bar{p}_{\widetilde{F}j}$ | 2.02475 | 2.00547 | 2.00140 | 2.00036 |
| | $\bar{p}_{Rj}$ | 2.01146 | 2.00287 | 2.00072 | 2.00018 |
| 20 | $\bar{p}_{Fj}$ | 2.00163 | 2.00030 | 2.00007 | 2.00003 |
| | $\bar{p}_{\widetilde{F}j}$ | 2.02560 | 2.00600 | 2.00152 | 2.00038 |
| | $\bar{p}_{Rj}$ | 2.01949 | 2.00487 | 2.00122 | 2.00030 |

**Table 3**
Order of accuracy for a sequence of meshes at $\tau = 0.76$.

| $\eta_\infty$ | $\bar{p}$ | $\Delta\eta$ (j) | | | |
|---|---|---|---|---|---|
| | | 1/8 (2) | 1/16 (3) | 1/32 (4) | 1/64(5) |
| 5 | $\bar{p}_{F,j}$ | 1.98228 | 1.99408 | 1.99835 | 1.99958 |
| | $\bar{p}_{\widetilde{F},j}$ | 2.02409 | 2.00325 | 2.00109 | 2.00072 |
| | $\bar{p}_{R,j}$ | 2.02194 | 2.00546 | 2.00137 | 2.00034 |
| 10 | $\bar{p}_{F,j}$ | 1.96106 | 1.98673 | 1.99629 | 1.99904 |
| | $\bar{p}_{\widetilde{F},j}$ | 2.02632 | 2.00573 | 2.00148 | 2.00039 |
| | $\bar{p}_{R,j}$ | 2.00655 | 2.00182 | 2.00048 | 2.00012 |
| 20 | $\bar{p}_{F,j}$ | 1.93980 | 1.98010 | 1.99449 | 1.99858 |
| | $\bar{p}_{\widetilde{F},j}$ | 2.02880 | 2.00687 | 2.00176 | 2.00045 |
| | $\bar{p}_{R,j}$ | 2.00062 | 2.00079 | 2.00027 | 2.00007 |

Next, we consider why it was necessary to use $\tau$, rather than $t$, for marching forward in time. Tables 4 and 5 show the order of accuracy of the scheme when $\tau = t^{1/2} = 1/\eta_\infty$; thus, we are judging the schemes on their performance before the outer extent of the lower deck reaches $\xi = 0$. From the tables, it is clear that the $t$-formulation provides very poor accuracy for the flux; on the other hand, the $\tau$-formulation provides excellent accuracy for all variables. We surmise that this is because the $t$-formulation contains $t^{1/2}$ and its derivatives, which are harder to capture with the regular Taylor expansions that are being used in a numerical scheme of this sort; on the other hand, there are no such square roots in the $\tau$-formulation.

Now, we consider the physical aspects of the results that were obtained. First of all, Fig. 2 compares the results for $\theta_s$ vs. $t$ obtained using the box scheme for three different meshes; the computations were carried out for $\eta_\infty = 5$, $\Delta\tau = 0.01/2^j$, $\Delta\eta = 0.5/2^j$, $\Delta\xi = 0.1/2^j$, for $j = 0, 1, 2$. Even though these results are for the three coarsest meshes considered, all solutions

**Table 4**
Order of accuracy for a sequence of meshes at $\tau = 1/\eta_\infty$.

| $\eta_\infty$ | $\bar{p}$ | $\Delta\eta$ (j) | | | |
|---|---|---|---|---|---|
| | | 1/8 (2) | 1/16 (3) | 1/32 (4) | 1/64 (5) |
| 5 | $\bar{p}_{G,j}$ | 2.00219 | 2.00055 | 2.00014 | 2.00003 |
| | $\bar{p}_{H,j}$ | 2.01226 | 2.00346 | 2.00084 | 2.00016 |
| | $\bar{p}_{R,j}$ | 1.97271 | 1.99321 | 1.99830 | 1.99958 |
| 10 | $\bar{p}_{G,j}$ | 2.00416 | 2.00105 | 2.00026 | 2.00007 |
| | $\bar{p}_{H,j}$ | 2.017999 | 2.00450 | 2.00111 | 2.00028 |
| | $\bar{p}_{R,j}$ | 1.97903 | 1.99475 | 1.99868 | 1.99967 |
| 20 | $\bar{p}_{G,j}$ | 2.01571 | 2.00392 | 2.00098 | 2.00024 |
| | $\bar{p}_{H,j}$ | 2.01786 | 2.00790 | 2.00197 | 2.00049 |
| | $\bar{p}_{R,j}$ | 1.99044 | 1.99742 | 1.99922 | 2.00069 |

**Table 5**
Order of accuracy for a sequence of meshes at $t = 1/\eta_\infty^2$.

| $\eta_\infty$ | $\bar{p}$ | $\Delta\eta$ (j) | | | |
|---|---|---|---|---|---|
| | | 1/8 (2) | 1/16 (3) | 1/32 (4) | 1/64 (5) |
| 5 | $\bar{p}_{G,j}$ | 1.98250 | 2.00432 | 2.00629 | 2.00627 |
| | $\bar{p}_{H,j}$ | 1.46906 | 1.36174 | 1.20769 | 0.62710 |
| | $\bar{p}_{R,j}$ | 1.97556 | 1.99765 | 2.00545 | 2.01143 |
| 10 | $\bar{p}_{G,j}$ | 1.98408 | 2.00455 | 2.00302 | 1.99861 |
| | $\bar{p}_{H,j}$ | 1.71753 | 1.56641 | 0.81915 | 0.53670 |
| | $\bar{p}_{R,j}$ | 1.98338 | 2.00950 | 2.02246 | 2.03500 |
| 20 | $\bar{p}_{G,j}$ | 1.97749 | 2.00359 | 1.99768 | 1.99777 |
| | $\bar{p}_{H,j}$ | 2.11246 | 1.54321 | 0.84738 | 0.55993 |
| | $\bar{p}_{R,j}$ | 2.06127 | 2.17436 | 2.32246 | 2.06266 |

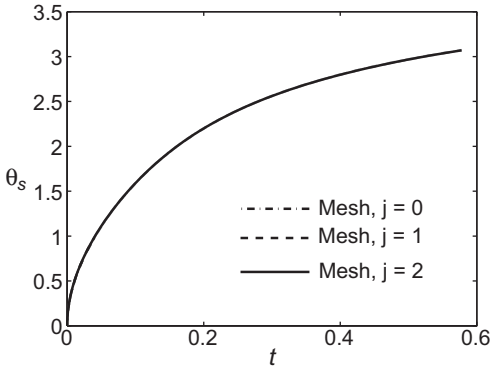


**Fig. 2.** Comparison of $\theta_s$ vs. $t$ obtained using the box scheme for three different meshes ($j = 0, 1, 2$). All solutions are virtually on top of each other.

are nonetheless virtually on top of each other, indicating that mesh-independence has been achieved. Next, Fig. 3 compares the result for $\theta_s$ for $j = 2$ from Fig. 2 with the solution of Sazhin et al. [23]. The numerical scheme used in [23] was based on the numerical solution of Eq. (5) combined with the analytical solution to Eq. (1), taking into account the changes in $R$ during the time steps. It was assumed that $R(t)$ is a linear function of $t$ during each time step, with the slope determined by Eq. (5) at the previous time step. An alternative approach to the solution to Eq. (1) has been suggested in [32]; in this approach, the solution to Eq. (1) was reduced to the solution of a Volterra integral equation of the second kind, and it was shown that the numerical schemes based on both solutions gave identical results, which confirms their correctness. Fig. 3 also displays the result obtained using the conventional numerical method, for which $R(t)$ is assumed to be piecewise constant in time; there is a clear discrepancy between this result and the others. Furthermore, the analysis in Section 4.1 indicates that $\theta_s \sim C_2 t^{1/2}$ initially, where $C_2$ is given in Eq. (35), which explains the sudden rise in $\theta_s$ just after $t = 0$ in Figs. 2 and 3.

Fig. 4 compares the results for $R(t)$ vs. $t$ obtained using the box scheme for the same three meshes as in Fig. 2; once again, mesh-independence is evident. Next, Fig. 5 compares the result for $R$ for $j = 2$ from Fig. 4 with the solutions computed by Sazhin et al. [23] for which $R(t)$ is assumed to be piecewise constant and piecewise linear in time; as in Fig. 3, the solution for which $R(t)$ is piecewise constant in time differs considerably from the others. Also, noting from Section 3 that $k_{gl} \ll 1$, $c_{gl} \ll 1$, we can understand why $R$ changes so slowly initially in Figs. 4 and 5.

The limit as $\tau \to \tau_e (= t_e^{1/2})$ turns out to be particularly interesting. First of all, it is evident that as this limit is approached, $R$ decreases very rapidly; hence, if $\Delta\tau$ is kept constant for the entire integration, as is necessary in order to compute the formal order of accuracy of the numerical scheme, it proves rather difficult to obtain solutions for $R$ that are close to zero; this issue can be partially resolved, however, by simply refining $\Delta\tau$. A more sophisticated resolution, which ensures that the numerical scheme can land at $R = 0$ when $\tau = \tau_e$ and with $\Delta\tau$ constant for the entire computation, is beyond the scope here, but is discussed in the conclusions.

Furthermore, the results of Sazhin et al. [23] indicate that, for given values of $T_0$ and $T_g$, the maximum surface temperature reached is always the same, regardless of the initial droplet radius. Note that this maximal temperature (wet-bulb temperature) is asymptotically approached only in the case when the contribution of thermal radiation is ignored; when this contribution is taken into account, the droplet temperature reaches its maximal temperature, which is greater than the wet-bulb temperature, and then decreases, approaching the wet-bulb temperature from above [33,34]. Fortunately, for the case of

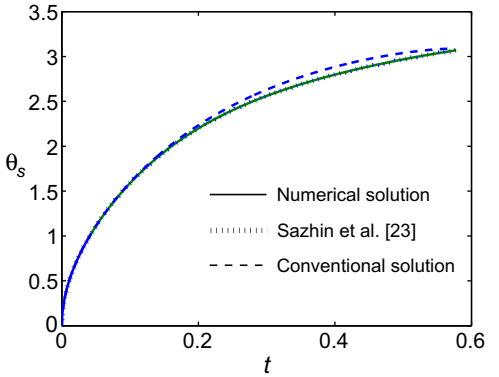


**Fig. 3.** Comparison of $\theta_s$ vs. $t$ obtained using three different methods: the box scheme for $j = 2$ (solid); the numerical method developed by Sazhin et al. [23] (dotted); and the conventional numerical method for which $R(t)$ is piecewise constant in time (dashed).

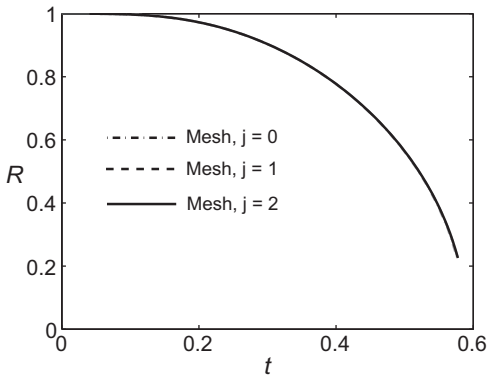


**Fig. 4.** Comparison of $R$ vs. $t$ obtained using the box scheme for three different meshes ($j = 0, 1, 2$). Once again, all solutions are virtually on top of each other.

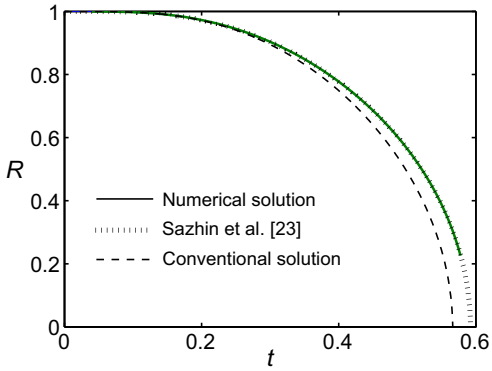


**Fig. 5.** Comparison of $R$ vs. $t$ obtained using three different methods: the box scheme for $j = 2$ (solid); the numerical method developed by Sazhin et al. [23] (dotted); and the conventional numerical method for which $R(t)$ is piecewise constant in time (dashed).

negligible thermal radiation, we are able analytically to investigate this further, as shown in the appendix. In brief, an analytical solution can be found as $t \to t_e$, and from this we are able to find the maximum surface temperature, in dimensional form, as $T_d + LD_1/c_l$, where $D_1$ is a constant that satisfies Eq. (A10); for the parameter values given in Table 1, we obtain 685.79 K, which is in excellent agreement with the value of 685.68 K obtained in our computations and that of 685.29 K obtained in [23]. This analysis is further backed up by the fact that $\dot{R}$ becomes very large and negative as $t \to t_e$, as is seen in Figs. 4 and 5, and Fig. 6, which shows the profiles for $F$ as a function of $\xi$ for different values of $t$, as $t \to t_e$; from the latter, it is evident that $F$ is tending to the expression given by (A11). Furthermore, Figs. 4 and 5 illustrate the potential peril of assuming *a priori* a piecewise linear expression for $R(t)$, since ultimately $R \sim (t_e - t)^{1/2}$.

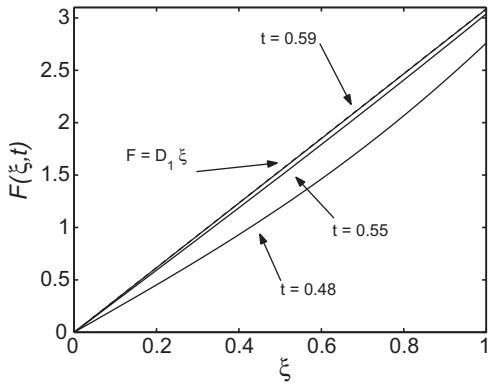


**Fig. 6.** $F$ vs. $\xi$ for three different values of $t$, as $t \to t_e$ (solid lines). The dashed line is the expression (A11).

## 6. Conclusions

This paper has considered the so-called boundary immobilization method, in tandem with the Keller box finite-difference scheme, for the numerical solution of a one-dimensional moving boundary problem arising during the transient heating of an evaporating droplet. An important component of the work was the use of variable transformations that must be built into the numerical algorithm in order to preserve second-order accuracy in both time and space for the temperature and the heat flux. This solution was found to agree well with that obtained using a recent alternative numerical scheme that employs an analytic solution of the linear heat conduction equation inside the droplet, for which the droplet radius was assumed to be a piecewise linear function of time [23]. In addition, we identified a canonical problem that can be solved once and for all for any initial droplet radius; this means that it could prove feasible to implement our method into CFD codes. Furthermore, as well as being formally more accurate than other methods, including that in [23], a further advantage of our algorithm is that it makes no assumptions about how the location of the front changes at each time-step and can be generalised to cases where the material properties vary with temperature, so that governing Eq. (1) is non-linear.

Whilst our combined analytical and numerical approach has explored most aspects of the problem, one issue that we have relegated to future work is whether it is possible to compute the time to total evaporation, $t_e$, with the same degree of accuracy as we have computed the temperature, the heat flux and the location of the moving boundary prior to $t_e$. This situation, where a phase is completely exhausted, occurs in a wide variety of Stefan problems [10,35–40], although, as far as we are aware, it is never treated particularly rigorously from the numerical point of view. The numerical method that we have presented here can therefore serve as a subroutine to an outer iterative loop whose role is to ensure the integration lands exactly at the value of $t$ at which $R = 0$, to some given tolerance, rather than either side of it, as is the case at present. To do this, whilst still keeping a uniform mesh for the purposes of checking the order of accuracy on a sequence of progressively finer meshes, will require us to be able to iterate for the step size used for the time variable. Since this is a complex task in the context of moving boundary problems, it would probably be wiser to perform numerical tests on a fixed boundary problem first, and a particular candidate for this would be the pre-solidification stage of the non-classical Stefan problem formulated in [8].

## Acknowledgements

The authors SLM and MV acknowledge the support of the Mathematics Applications Consortium for Science and Industry (www.macsi.ul.ie) funded by the Science Foundation Ireland Mathematics Initiative Grant 06/MI/005. The authors IGG and SSS are grateful to the European Regional Development Fund Franco-British INTERREG IVA (Project C5, Reference 4005) for the financial support of this project.

## Appendix A

A limit of particular interest is that for total evaporation time when $R$ reaches zero. Consider the possibility that

$$R(t) \sim \lambda(t_e - t)^{\alpha}, \tag{A1}$$

where $\lambda$ and $\alpha$ are strictly positive constants whose values we hope to determine; this analysis cannot, however, give any indication of the value of $t_e$. Choosing $\alpha = 1/2$ gives that, in the limit as $t \to t_e$, or $\tau \to \tau_e$, (21) becomes

$$\frac{\partial^2 F}{\partial \xi^2} = -\frac{1}{2}\lambda^2 F + \frac{1}{2}\lambda^2 \xi \frac{\partial F}{\partial \xi}, \tag{A2}$$

subject to

$$\frac{\partial F}{\partial \xi} + (k_{gl} - 1)F = k_{gl}\theta_g - \frac{1}{2}\lambda^2 \quad \text{at } \xi = 1, \tag{A3}$$

$$-\frac{1}{2}\lambda^2 = -c_{gl}k_{gl}\ln(1 + B_{M,e}) \quad \text{at } \xi = 1, \tag{A4}$$

$$F = 0 \quad \text{at } \xi = 0, \tag{A5}$$

where

$$B_{M,e} = \frac{M_f P_{fs,e}}{M_g(P_g - P_{fs,e})} \tag{A6}$$

with

$$P_{fs,e} = \exp\left(a - \frac{\beta}{F(1, t_e) + \gamma}\right).$$

The general solution to (A2) is now

$$F = D_1\xi + D_2\left(\frac{1}{2}\lambda^2\xi\int_0^{\xi} e^{\lambda^2\hat{\xi}^2/4}\,d\hat{\xi} - e^{\lambda^2\xi^2/4}\right), \tag{A7}$$

where $D_1$ and $D_2$ are constants to be determined. Applying (A5) it follows that $D_2 = 0$, and then (A3) and (A4) give, respectively,

$$k_{gl}D_1 = k_{gl}\theta_g - \frac{1}{2}\lambda^2, \tag{A8}$$

$$-\frac{1}{2}\lambda^2 = -c_{gl}k_{gl}\ln(1 + B_{M,e}), \tag{A9}$$

resulting in a transcendental equation for $D_1$:

$$\left(\exp\left(\frac{\theta_g - D_1}{c_{gl}}\right) - 1\right)\left(P_g\exp\left(\frac{\beta}{D_1 + \gamma} - a\right) - 1\right) = \frac{M_f}{M_g}. \tag{A10}$$

Note that even though the solution that we have found, i.e.

$$F = D_1\xi, \tag{A11}$$

would have satisfied (21) in the limit as $t \to t_e$ if we had chosen $\alpha > 1/2$ or $\alpha < 1/2$, the equation set would have been inconsistent, since the left-hand side of (23) would have been zero or infinite, respectively, and it would not have been possible to satisfy this boundary condition; thus, $\alpha = 1/2$ is the only possible choice.

## References


[1] J. Caldwell, Y.Y. Kwan, Numerical methods for one-dimensional Stefan problems, Commun. Numer. Methods Eng. 20 (2004) 535–545.
[2] J. Caldwell, S. Savović, Numerical solution of Stefan problem by variable space grid and boundary immobilization method, J. Math. Sci. 13 (2002) 67–79.
[3] J. Caldwell, Y.Y. Kwan, Starting solutions for the boundary immobilization method, Commun. Numer. Methods Eng. 21 (2005) 289–295.
[4] S. Savović, J. Caldwell, Finite-difference solution of one-dimensional Stefan problem with periodic boundary conditions, Int. J. Heat Mass Transfer 46 (2003) 2911–2916.
[5] S. Kutluay, A.R. Bahadir, A. Ozdes, The numerical solution of one-phase classical Stefan problem, J. Comput. Appl. Math. 81 (1) (1997) 135–144.
[6] P.C. Meek, J. Norbury, Nonlinear moving boundary problems and a Keller box scheme, SIAM J. Numer. Anal. 21 (5) (1984) 883–893.
[7] S.L. Mitchell, M. Vynnycky, Finite-difference methods with increased accuracy and correct initialization for one-dimensional Stefan problems, Appl. Math. Comput. 215 (2009) 1609–1621.
[8] M. Vynnycky, S.L. Mitchell, On the solution of Stefan problems with delayed onset of phase change, presented at HEFAT2010, in: 7th International Conference on Heat Transfer, Fluid Mechanics and Thermodynamics, 19–21 July 2010, Antalya, Turkey, 2010, pp. 709–714.
[9] A. Esen, S. Kutluay, A numerical solution of the Stefan problem with a Neumann-type boundary condition by enthalpy method, Appl. Math. Comput. 148 (2) (2004) 321–329.
[10] J. Caldwell, C.-C. Chan, Spherical solidification by the enthalpy method and the heat balance integral method, Appl. Math. Model. 24 (2000) 45–53.
[11] F. Liu, D.L.S. McElwain, A computationally efficient solution technique for moving-boundary problems in finite media, IMA J. Appl. Math. 59 (1) (1997) 71–84.
[12] Rizwan-uddin, A nodal method for phase change moving boundary problems, Int. J. Comput. Fluid Dyn. 11 (1999) 211–221.
[13] J. Caldwell, C.K. Chiu, Numerical solution of one-phase Stefan problems by the heat balance integral method. Part I – Cylindrical and spherical geometries, Commun. Numer. Methods Eng. 16 (2000) 569–583.
[14] J. Caldwell, C.K. Chiu, Numerical solution of one-phase Stefan problems by the heat balance integral method. Part II – Special small time starting procedure, Commun. Numer. Methods Eng. 16 (2000) 585–593.
[15] T.R. Goodman, The heat-balance integral and its application to problems involving a change of phase, Trans. ASME 80 (1958) 335–342.
[16] S.L. Mitchell, T.G. Myers, A heat balance integral method for one-dimensional finite ablation, AIAA J. Thermophys. 22 (2) (2008) 508–514.
[17] S.L. Mitchell, T.G. Myers, Approximate solution methods for one-dimensional solidification from an incoming fluid, Appl. Math. Comput. 202 (1) (2008) 311–326.
[18] T.G. Myers, S.L. Mitchell, G. Muchatibaya, M.Y. Myers, A cubic heat balance integral method for one-dimensional melting of a finite thickness layer, Int. J. Heat Mass Transfer 50 (2007) 5305–5317.
[19] T.G. Myers, Optimizing the exponent in the heat balance and refined integral methods, Int. Commun. Heat Mass Transfer 36 (2) (2009) 143–147.
[20] S.L. Mitchell, T.G. Myers, Application of standard and refined heat balance integral methods to one-dimensional Stefan problems, SIAM Rev. 52 (1) (2010) 57–86.
[21] S.S. Sazhin, P.A. Krutitskii, W.A. Abdelghaffar, E.M. Sazhina, S.V. Mikhalovsky, S.T. Meikle, M.R. Heikal, Transient heating of diesel fuel droplets, Int. J. Heat Mass Transfer 47 (2004) 3327–3340.
[22] S.S. Sazhin, Advanced models of fuel droplet heating and evaporation, Prog. Energy Combust. Sci. 32 (2) (2006) 162–214.
[23] S.S. Sazhin, P.A. Krutitskii, I.G. Gusev, M.R. Heikal, Transient heating of an evaporating droplet, Int. J. Heat Mass Transfer 53 (2010) 2826–2836.
[24] M. Vynnycky, Concerning closed-streamline flows with discontinuous boundary conditions, J. Eng. Math. 33 (1998) 141–156.
[25] S.S. Sazhin, I.N. Shishkova, A.P. Kryukov, V.Y. Levashov, M.R. Heikal, Evaporation of droplets into a background gas: kinetic modelling, Int. J. Heat Mass Transfer 50 (2007) 2675–2691.
[26] S.S. Sazhin, I.N. Shishkova, A kinetic algorithm for modelling the droplet evaporation process in the presence of heat flux and background gas, Atom. Sprays 19 (5) (2009) 473–489.
[27] T. Cebeci, F. Thiele, P.G. Williams, K. Stewartson, On the calculation of symmetric wakes. I – Two-dimensional flows, Numer. Heat Transfer 2 (1979) 35–60.
[28] J.C. Strikwerda, Finite Difference Schemes and Partial Differential Equations, second ed., Society for Industrial Mathematics, 2004.
[29] T. Cebeci, P. Bradshaw, Momentum Transfer in Boundary Layers, Hemisphere Publishing Corporation, Washington, 1977.
[30] T. Cebeci, P. Bradshaw, Physical and Computational Aspects of Convective Heat Transfer, Springer, Verlag, 1984.
[31] T. Cebeci, J. Cousteix, Modeling and Computation of Boundary-Layer Flows, Springer, 2005.
[32] S.S. Sazhin, I.N. Shishkova, I.G. Gusev, A. Elwardnay, P.A. Krutitskii, M. Heikal, Fuel droplet heating and evaporation: new hydrodynamic and kinetic models, in: Proceedings of the 14th International Heat Transfer Conference, IHTC14-22320, 2010.
[33] B. Abramzon, S.S. Sazhin, Droplet vaporization model in the presence of thermal radiation, Int. J. Heat Mass Transfer 48 (2005) 1868–1873.

[34] B. Abramzon, S.S. Sazhin, Convective vaporization of fuel droplets with thermal radiation absorption, Fuel 85 (1) (2006) 32–46.
[35] J. Åberg, M. Vynnycky, H. Fredriksson, Heat-flux measurements of industrial on-site continuous copper casting and their use as boundary conditions for numerical simulations, Trans. Ind. Inst. Met. 62 (2009) 443–446.
[36] M. Vynnycky, A mathematical model for air-gap formation in vertical continuous casting: the effect of superheat, Trans. Ind. Inst. Met. 62 (2009) 495–498.
[37] M. Vynnycky, The cooling of a water droplet and the Mpemba effect, in: 21st International Symposium on Transport Phenomena, Kaohsiung City, Taiwan (CD-ROM), 2010, pp. 1404–1410.
[38] A.P. Roday, M.J. Kazmierczak, Analysis of phase-change in finite slabs subjected to convective boundary conditions. Part I – Melting, Int. Rev. Chem. Eng. (Rapid Commun.) 1 (2009) 87–99.
[39] A.P. Roday, M.J. Kazmierczak, Analysis of phase-change in finite slabs subjected to convective boundary conditions. Part II – Freezing, Int. Rev. Chem. Eng. (Rapid Commun.) 1 (2009) 100–108.
[40] A.P. Roday, M.J. Kazmierczak, Melting and freezing in a finite slab due to a linearly decreasing free-stream temperature of a convective boundary condition, Thermal Sci. 2 (2009) 141–153.